

Evidence for Non-smooth Quenching in Massive Galaxies at $z \sim 1$

Timothy Carleton^{1*}, Yicheng Guo¹, Hooshang Nayyeri², Michael Cooper²,
Gregory Rudnick³, Katherine Whitaker^{4, 5}

¹Department of Physics and Astronomy, 223 Physics Building, University of Missouri, Columbia, MO 65211, USA

²Center for Cosmology, Department of Physics and Astronomy, 4129 Reines Hall, University of California, Irvine, CA 92697, USA

³The University of Kansas, Department of Physics and Astronomy, Malott Room 1082, 1251 Wescoe Hall Drive, Lawrence, KS, 66045, USA

⁴Department of Physics, University of Connecticut, Storrs, CT 06269, USA

⁵Department of Astronomy, University of Massachusetts, 710 North Pleasant St, LGRT-524, Amherst, MA 01003, USA

31 October 2019

ABSTRACT

We investigate a large sample of massive galaxies at $z \sim 1$ with combined *HST* broad-band and grism observations to constrain the star-formation histories of these systems as they transition from a star-forming state to quiescence. Among our sample of massive ($M_* > 10^{10} M_\odot$) galaxies at $0.7 < z < 1.2$, dust-corrected $H\alpha$ and UV star-formation indicators agree with a small dispersion (~ 0.2 dex) for galaxies on the main sequence, but diverge and exhibit substantial scatter (~ 0.7 dex) once they drop significantly below the star-forming main sequence. Significant $H\alpha$ emission is present in galaxies with low dust-corrected UV SFR values as well as galaxies classified as quiescent using the *UVJ* diagram. We compare the observed $H\alpha$ flux distribution to the expected distribution assuming bursty or smooth star-formation histories, and find that massive galaxies at $z \sim 1$ are most consistent with a quick, bursty quenching process. This suggests that mechanisms such as feedback, stochastic gas flows, and minor mergers continue to induce low-level bursty star formation in massive galaxies at moderate redshift, even as they quench.

Key words: galaxies: formation, evolution, starburst, high-redshift, ISM, ultraviolet: galaxies

1 INTRODUCTION

A growing consensus of observations indicates that the population of massive quiescent galaxies has been building up since before $z = 3$ (Bell et al. 2004; Faber et al. 2007; Ilbert et al. 2013). The presence of this population at early epochs poses a significant challenge to our current understanding of galaxy formation and evolution, as these systems must have formed early and suffered a quick shutdown in star formation (‘quenching’; Peng et al. 2010; Thomas et al. 2010; Kuntschner et al. 2010; van Dokkum et al. 2015; Daddi et al. 2005; Goddard et al. 2017). Many mechanisms have been proposed to cause this shutdown of star formation in massive galaxies, such as the build-up of a hot-gas halo (Kereš et al. 2005; Dekel & Birnboim 2006), feedback from an Active-Galactic-Nucleus (AGN; Di Matteo et al. 2005; Hopkins et al. 2006; Beckmann et al. 2017) or star formation activity (Oppenheimer & Davé 2006; Ceverino & Klypin 2009) driven by a recent merger (Hopkins et al. 2014), or the stabilization of the cold gas against fragmentation (Martig et al. 2009). However, the importance/feasibility of these processes, and how they may evolve with redshift, is still uncertain and remains a major unanswered question in our current understanding of galaxy evolution.

As many authors have noted (Martin et al. 2007; Schawinski et al. 2014; Wild et al. 2016; Belfiore et al. 2016; Pandya et al. 2017), understanding of the processes involved in quenching can be discerned through detailed studies of massive galaxies in the process of transitioning from star-forming to quiescent. Determining the star-formation histories of these galaxies can constrain which processes drive quenching. For example, Schawinski et al. (2007) found that local early-type galaxies are consistent with a short (< 250 Myr) quenching associated with merger-driven feedback, but late-type galaxies are consistent with a longer (many Gyr) quenching process such the buildup of a hot gas halo through radio-mode AGN feedback (Croton et al. 2006). Similarly, by using semi-analytic models describing the star-formation histories of massive galaxies, Pandya et al. (2017) found that a fast quenching mode is the predominant quenching mode at high z , whereas low- z galaxies are associated with a slower quenching process. At $z = 1.4 - 2.6$, Zick et al. (2018) investigate the spectra of transition galaxies at, finding that quenching occurs on a $100 - 200$ Myr timescale, and using photometric data of galaxies between $z = 0.25$ and $z = 3.75$, Carnall et al. (2018) find that most massive galaxies are consistent with quenching times $\lesssim 1$ Gyr. Studies investigating the abundance of galaxies with SFRs in between the star-forming and quiescent populations over cosmic time find that quenching takes place on

* e-mail: carleton@missouri.edu

$\sim 1 - 3$ Gyr timescales (Wetzell et al. 2013; Balogh et al. 2004; Hahn et al. 2017).

However, the photometric signatures relied upon by these studies are predominantly sensitive to B and A stars tracing the average SFR in the past few hundred Myr — any 10 – 100 Myr variations don't leave an imprint on them (Worthey & Ottaviani 1997). A growing body of evidence suggests that star formation in low-mass galaxies is dominated by episodes of bursty star-formation activity where the instantaneous SFR can vary by nearly an order of magnitude on ~ 10 Myr timescales (Guo et al. 2016; Weisz et al. 2012; Sparre et al. 2017). Whether massive galaxies experience this same level of burstiness as they quench can help elucidate the processes at play as their star-formation activity shuts down (French et al. 2018).

This bursty star-formation activity is usually identified through the ratio of $H\alpha$ and UV star-formation indicators. Nebular emission from HII regions around O stars lasting ~ 10 Myr closely traces the immediate SFR, whereas UV emission from B and A stars lasting ~ 200 Myr traces the average SFR over longer timescales. In depth studies have shown that $H\alpha$ and UV tracers agree for galaxies with ongoing star formation at a level above $0.1 M_{\odot} \text{ yr}^{-1}$ in the local Universe (Salim et al. 2007; Fumagalli et al. 2011) and above $10 M_{\odot} \text{ yr}^{-1}$ at higher redshifts (Reddy et al. 2010; Shivaei et al. 2015, but see Wisnioski et al. 2019). Deviations from this agreement have been used as evidence for bursty star-formation activity in dwarf galaxies (Guo et al. 2016; Weisz et al. 2012). Indeed, simulations of star-formation in low-mass galaxies find that the $H\alpha/UV$ luminosity ratio varies in a way consistent with the assumed bursty nature of star formation (Sparre et al. 2017). However, these results are generally limited to low-mass galaxies with high specific SFRs. It is unclear if *high-mass* galaxies with *low specific SFRs* show this behavior as well.

In this paper, we present evidence of bursty star formation in massive transition galaxies (galaxies more than 1 dex below the main sequence, but not completely quenched) at $z \sim 1$, suggesting that these galaxies experience a bursty decline in star-formation activity, rather than a smooth one. In section 2, we describe our sample selection and SFR measurements. In section 3, we compare the observed $H\alpha$ and UV SFRs and describe the model SFHs used in our analysis. In section 4 we compare our measurements with the predictions of the model SFHs, and in section 5 we describe possible systematic effects on our results. Section 6 summarizes our conclusions. Throughout this study, we assume a Λ CDM cosmology with $H_0 = 70 \text{ km s}^{-1} \text{ Mpc}^{-1}$, $\Omega_m = 0.3$, and $\Omega_{\Lambda} = 0.7$. Except for when otherwise indicated, we assume a Chabrier (2003) IMF.

2 DATA

Our data is primarily drawn from the 3D-HST survey (Skelton et al. 2014; Momcheva et al. 2016). This survey targets the CANDELS fields (Grogin et al. 2011; Koekemoer et al. 2011) with the G141 grism, which covers 1.1 to 1.65 μm and traces $H\alpha$ emission between $z = 0.7$ to $z = 1.5$. We make use of stellar masses, rest-frame colors, $H\alpha$ fluxes, and redshifts published in the 3D-HST catalogs. The derivation of these parameters is described in detail in Momcheva et al. (2016). Below, we briefly summarize these calculations.

First, accompanying JH_{F140W} and H_{F160W} direct-exposure images have been used to identify all objects in the 3D-HST footprint with $JH_{F140W} < 26$. Images were reduced with the CALWF3 package, and grism spectra were extracted utilizing the AXE pipeline, using direct exposure images for source extraction

and contamination estimation. Photometry was carried out on the direct-exposure images and combined with publicly-available optical and near-IR photometry to create observed spectral energy distributions (SEDs). These SEDs were fit with template SEDs to measure the photometric redshift (using EAZY; Brammer et al. 2008) and theoretical SEDs to determine the stellar mass (using FAST; Kriek et al. 2009). Rest-frame colors were determined by fixing the template redshift at the best-fit redshift (Z_{BEST}) and refitting the SED to the photometry, only using observed filters, i , for which $|\lambda_{\text{obs},i} - \lambda_{\text{rest},j}| < 1000 \text{ \AA}$ and measuring the flux through the rest-frame filter j .

In our sample we select from the 1754 galaxies for which the 3D-HST catalogs contain a measurement of the $H\alpha$ flux, have a stellar mass (M_*) above $10^{10} M_{\odot}$, and are between z of 0.7 and 1.2. These limits are identified so that $H\alpha$ is detectable well below the main sequence: the 3σ $H\alpha$ detection limit taken from Momcheva et al. (2016) reaches 1.3 dex below the main sequence at $z = 1.2$ for point sources with no extinction. Additionally, we make the following cuts to our sample:

- (i) We exclude 112 X-ray detected AGN identified in the CANDELS catalogs (Ueda et al. 2008; Salvato et al. 2011; Xue et al. 2011; Rangel et al. 2013; Nandra et al. 2015) from our sample.
- (ii) Because accurate rest-frame UV luminosities, which are derived from the UV portion of the best-fit SED, are critical to this analysis, we further restrict our sample to objects with good photometry (as determined by the USE_PHOT flag in the 3D-HST catalog), excluding 97 objects. We also exclude 486 predominantly star-forming objects where the reduced χ^2 of the best-fit SED is greater than 2. Many objects with poor SED fits either have a nearby companion or a disturbed morphology, suggesting that inconsistent aperture photometry is the cause of the high χ^2 values.
- (iii) To ensure accurate $H\alpha$ measurements, 14 objects are excluded for which the grism coverage is incomplete within 100 \AA of $H\alpha$ at the best-fit redshift.
- (iv) To avoid spurious $H\alpha$ measurements, we exclude 2 objects for which the contamination level is more than 50% of the total flux and 47 for which the contamination at the wavelength of $H\alpha$ is $> 50\%$.
- (v) For galaxies whose dust-corrected UV SFRs (see Sec. 2.1) are at least 1 dex below the main sequence, we visually inspect both the 1D and 2D grism spectra to verify that the emission is not due to contamination, a bad redshift, or any anomalies in the spectrum, removing 17 additional objects.
- (vi) Because constraints on the level of extinction from SED fitting in the CANDELS catalogs are necessary to accurately correct our measurements for dust extinction, we exclude the 216 objects in the GOODS-N field, as the CANDELS-based SED-fitting in that field is not complete.

These cuts leave 780 galaxies overall, 417 of which have $H\alpha$ emission above the 3σ level. All objects have at least one observation blue-ward of rest-frame 2800 \AA , and 88% of objects have least one detection in that wavelength range, so the NUV luminosity is well constrained by observations.

Figure 1 illustrates this sample in the UVJ diagram, as well as a diagram showing the sample in M_* vs. dereddened ($U - V$) space. The observed $U - V$ colors are dereddened using a Calzetti et al. (2000) extinction law and extinction from the best-fit SED in the CANDELS catalogs (see Sec. 2.1). Figure 2 shows the sample in $\text{SFR} - M_*$ space. In both figures, points are color-coded by the ra-

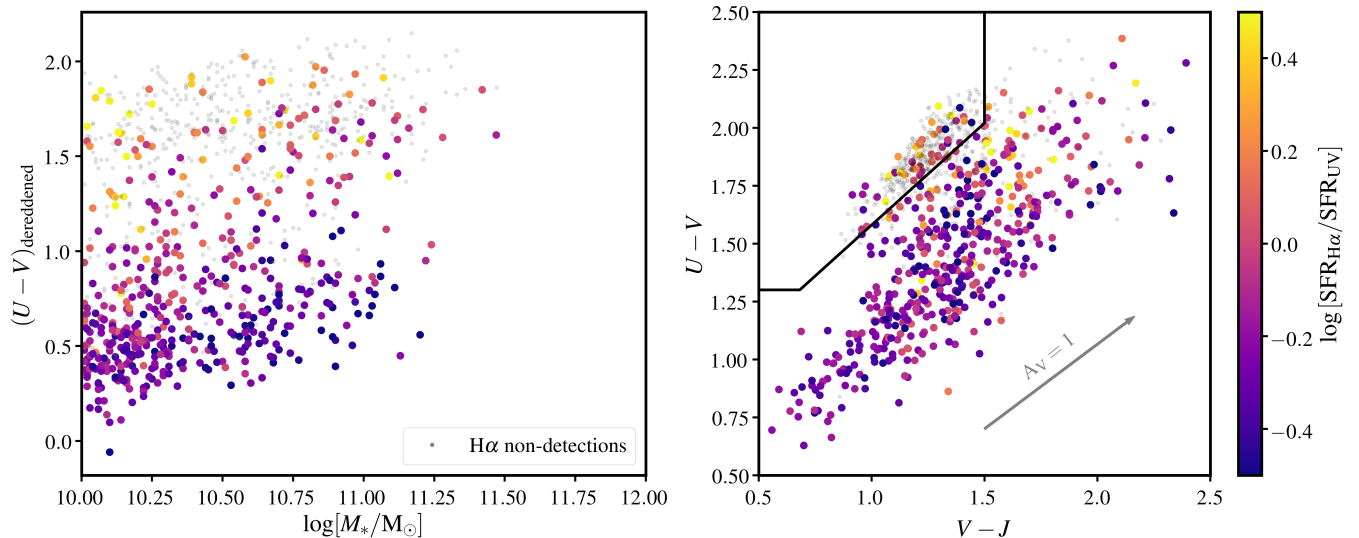


Figure 1. Our sample in both M_* -vs-dereddened $U - V$ space (left) and the UVJ -diagram (right). For objects with $H\alpha$ detections, the color of the point corresponds to the ratio between $H\alpha$ and UV SFRs. While $H\alpha$ -detected objects are primarily blue, continuously star-forming objects, there is a significant population of red, quiescent galaxies with $H\alpha$ SFRs comparable to their UV SFRs.

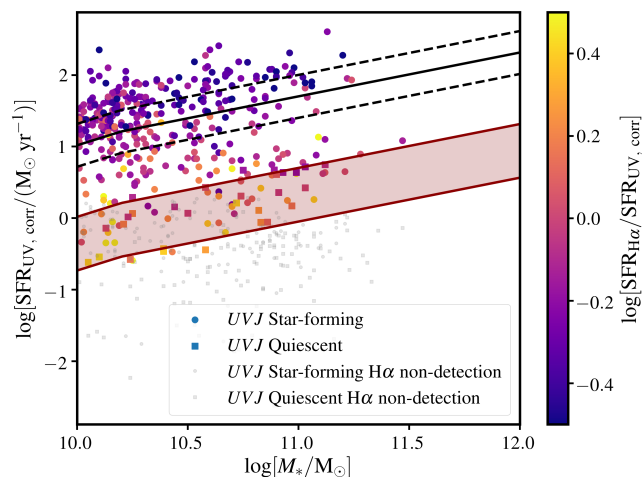


Figure 2. Our sample in SFR - M_* space. As in Figure 1, objects with $H\alpha$ emission are color-coded by the ratio of their $H\alpha$ and UV SFRs and grey points show objects with $H\alpha$ non-detections. Points and squares show objects classified as UVJ star-forming and UVJ -quiescent respectively. The black solid and dashed lines show the main sequence from (Whitaker et al. 2014) and 0.3 dex scatter respectively. The red shaded region corresponds to between 1 and 1.75 dex below the main sequence, where we focus our investigation. While the ratio of UV-to- $H\alpha$ SFR is uniform for objects on the main sequence, there is a substantial variation for objects below the main sequence.

tio between $H\alpha$ and UV SFRs for objects with $H\alpha$ emission. It is already clear that, while most objects with $H\alpha$ emission are classified as star-forming, 11% of UVJ -quiescent objects and 20% of objects more than 1 dex below the main sequence have significant $H\alpha$ emission. To specifically investigate the nature of the SFH of galaxies in the process of quenching, we narrow our focus further to the 312 systems (92 of which are UVJ -star forming and 220 of which are UVJ -quiescent) whose dust-corrected UV SFRs are be-

tween 1 and 1.75 dex below the main sequence of Whitaker et al. (2014) in our modeling (Section 3). This space is highlighted in Figure 2.

2.1 SFR measurements

The UV-based SFR, which is sensitive to stars less than 100 – 200 Myr old, is derived from the UV luminosity at 2800 Å following the Wuyts et al. (2011) conversion:

$$\log(\text{SFR}_{\text{UV}}) = \log(L_{2800}) - 9.44 + 0.4A_{\text{UV}}, \quad (1)$$

where SFR_{UV} is the dust-corrected UV SFR in units of $M_{\odot} \text{ yr}^{-1}$ and L_{2800} is the luminosity at 2800 Å in units of L_{\odot} taken from the best-fit SED. We assume a Calzetti et al. (2000) extinction law, such that $A_{\text{UV}} = 7.26E(B - V)$, where $E(B - V)$ is the V -band reddening. Because low-SFR galaxies (at least 1 dex below the main sequence) in our analysis have relatively little dust ($E(B - V) \sim 0.1$), the adoption of an alternative extinction law has a negligible effect on our results. For example, adopting an SMC law (Gordon et al. 2003) alters the UV SFRs by < 0.1 dex and the ratio between UV and $H\alpha$ SFRs by < 0.1 dex for 90% of low-SFR objects. Deep imaging from *HST*, the CFHT, and Subaru telescope sample this region of the SED to a 3σ depth of approximately 27.5, resulting in an unobscured SFR limit of $\sim 0.3 M_{\odot} \text{ yr}^{-1}$ at $z = 1.2$.

At high redshifts, a majority of the UV light from star-formation is absorbed and re-emitted in the far-IR (Whitaker et al. 2014). While far-IR measurements from *Herschel* or ground-based sub-mm telescopes can measure this directly for a limited number of bright objects, most survey-based studies rely on a luminosity-dependent conversion from *Spitzer* 24 μm flux to a total IR luminosity (Whitaker et al. 2014, 2017). However, diffuse dust heated from old stars, in addition to emission directly from asymptotic-giant branch (AGB) stars, can contribute substantially to the observed 24 μm flux for galaxies with low SFRs (Piovan et al. 2003; Marigo et al. 2008; Kelson & Holden 2010; Fumagalli et al. 2014). Additionally the conversion between polycyclic aromatic hydrocarbon (PAH) emission (the origin of 24 μm emission at high z) and

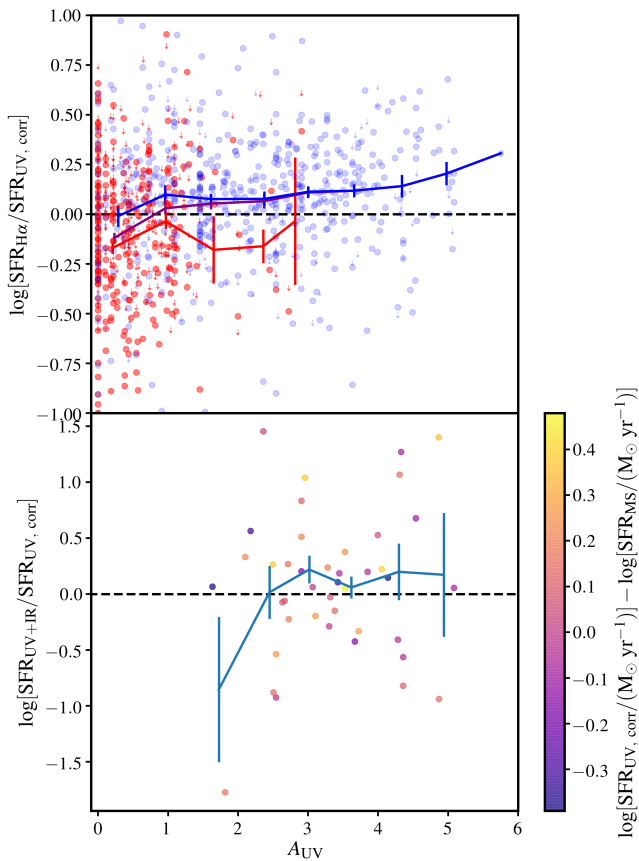


Figure 3. Verification of our extinction measurements. **Top:** The upper plot shows the ratio of H α -to-UV SFR as a function of A_{UV} , with *UVJ*-quiescent objects shown as red points and *UVJ*-star forming objects shown as blue points. Although *UVJ*-quiescent objects have lower H α /UV SFRs than *UVJ*-star-forming objects (see Sec. 4), there is no correlation between extinction and H α /UV SFR. This implies that our assumed ratio of nebular-to-continuum extinction is not affecting our H α SFR values. **Bottom:** The ratio UV+IR SFRs with *Herschel* detections to our dust-corrected UV SFRs. Objects in this plot are further restricted to objects whose UV-corrected SFRs are $> 20 M_{\odot} \text{ yr}^{-1}$ to avoid selection effects. Points are color-coded by offset from the main sequence. The SFR measurements agree and there is no correlation with A_{UV} or distance from the main sequence, suggesting that our dust-corrected UV SFRs are accurate.

SFR depends on the age and ionizing flux of the stellar population (Shivaei et al. 2017), which may vary significantly across our sample.

Given these uncertainties, we elect to use the UV luminosity corrected for extinction, which primarily derives from young stars, to measure the star-formation activity on these timescales. By comparing our dust-corrected UV SFRs with *Herschel*-based SFRs available for a subset of our sample (142 objects, 42 of which have dust-corrected UV SFRs greater than $20 M_{\odot} \text{ yr}^{-1}$), we have determined that using the extinction reported in the 3D-HST catalogs results in a correlation between extinction and the ratio of *Herschel*-based SFRs-to-dust-corrected UV SFRs, even among galaxies for which *Herschel* observations are complete. Alternatively, using the median $E(B - V)$ reported in the CANDELS catalogs, combining 14 different SED fits with different assumptions (Nayyeri et al. 2017; Stefanon et al. 2017; Guo et al. 2013; Galametz et al. 2013), results in agreement between the UV-corrected SFRs and UV+IR

SFRs within 50% and independent of the amount of extinction for objects with UV-corrected SFRs greater than $20 M_{\odot} \text{ yr}^{-1}$ (see Fig. 3). Moreover, Balmer-decrement-based extinction measurements for objects in the LEGA-C survey (van der Wel et al. 2016) agree with the CANDELS extinction measurement better than the 3D-HST measurement. The UV-corrected SFRs agree with the SFR of the best-fit SED for star-forming objects, further suggesting that the dust-corrected UV SFRs are accurate. For objects with low SFRs, the above recipe may overestimate their true SFRs because emission from Post-AGB stars, Blue-Horizontal-Branch Stars, and Blue Stragglers can represent a non-negligible fraction of the UV luminosity (Dorman et al. 1995). Because this emission depends on the SFH of the galaxy in a non-trivial way, we incorporate it into our modeling (see Sec. 3 and 5.1.2) rather than subtracting this emission when calculating the UV SFR.

The H α -based SFRs ($\text{SFR}_{H\alpha}$) are calculated from the Kennicutt & Evans (2012) conversion adjusted to a Chabrier IMF following Muzzin et al. (2010):

$$\log(\text{SFR}_{H\alpha}) = \log(L_{H\alpha}) - 7.77 + 0.4A_{H\alpha}, \quad (2)$$

where $L_{H\alpha}$ is the luminosity of the H α line in solar luminosities, and $A_{H\alpha}$ is the internal extinction of the H α line. The 3σ H α flux limit achieved by 3D-HST of $2.1 \times 10^{-17} \text{ erg/s/cm}^2$ corresponds to a H α SFR of $0.8 M_{\odot} \text{ yr}^{-1}$ at $z = 1.2$ assuming $A_{H\alpha} = 0$. To accurately measure H α SFRs, we correct the H α luminosity for (1) extinction, (2) stellar absorption, (3) emission from post-AGB stars, and (4) contamination from nearby [NII] emission (in that order).

The H α SFRs are corrected for extinction following a Calzetti et al. (2000) law. Following Wuyts et al. (2013), we relate the nebular extinction to the continuum emission as $A_{H\alpha} = 1.9A_{\text{cont}} - 0.15A_{\text{cont}}^2$, where A_{cont} is the continuum extinction at H α . For a subsample (13) of objects with H β detections from the LEGA-C survey (van der Wel et al. 2016), the Balmer-decrement-based extinction measurements are generally consistent with the extinction determined from the continuum extinction, with a median deviation of 0.32 mag and dispersion of 1.2 mag. Among these objects, there is no correlation between the deviation and the measured extinction.

We correct for H α absorption, which can be significant for massive galaxies (Kauffmann et al. 2003), using an age-dependent factor based on the amount of absorption in spectra generated following the model SFHs used in our analysis (see Sec. 3). On average, for our star-formation histories, this varies with age according to:

$$\log(\text{H}\alpha \text{ EW}) = \begin{cases} 0.431 & t_{\text{LW}} < 6 \times 10^8 \text{ Gyr} \\ -0.11(\log t_{\text{LW}})^2 + 0.18(\log t_{\text{LW}}) + 0.53 & t_{\text{LW}} > 6 \times 10^8 \text{ Gyr} \end{cases} \quad (3)$$

where H α EW is the H α equivalent width of absorption and t_{LW} is the bolometric light-weighted age of the stellar population in Gyr. For each galaxy, the light-weighted age from the 3D-HST catalog is used in conjunction with Equation 3 to determine the amount of H α absorption. However, if a constant absorption of 3 \AA is adopted, the change in our results is negligible. For star-forming galaxies, this correction lowers the sSFR by $\sim 10^{-10.3} \text{ yr}^{-1}$; for older quiescent galaxies, it corresponds to a decrease of $\sim 10^{-10.8} \text{ yr}^{-1}$.

Furthermore, post-AGB stars can produce enough ionizing radiation to contribute significantly to the H α luminosity (Cid Fernandes et al. 2011; Singh et al. 2013; Belfiore et al.

2016). Although there remains uncertainty with regard to the specifics of AGB and post-AGB stellar evolution, models generally agree that evolved stars provide an ionizing flux of $\sim 10^{41}$ photons/s/ M_{\odot} (Cid Fernandes et al. 2011) independent of age. Assuming Case-B recombination and a temperature of 10,000 K, this corresponds to a $H\alpha$ luminosity per stellar mass of 1.37×10^{29} erg s $^{-1}$ M_{\odot}^{-1} . Given that evolved stellar-populations have $[NII]/H\alpha$ ratios close to 1 (Belfiore et al. 2016), we subtract $2 \times 1.37 \times 10^{29} \times (M_*/M_{\odot})$ erg s $^{-1}$ (corresponding to a sSFR of 1.2×10^{-12} yr $^{-1}$) from the $H\alpha$ luminosity to isolate the $H\alpha$ emission associated with young stars.

Because of the low spectral resolution of the grism, the measured $H\alpha$ flux contains emission from both $H\alpha$ and nearby $[NII]$. To correct for this contamination, we adopt a mass-dependent correction motivated by the mass-metallicity relation. The gas-phase metallicity is estimated from the measured stellar mass assuming the redshift-dependent mass-metallicity relation of Zahid et al. (2014), and the metallicity is converted to a $[NII]/H\alpha$ flux ratio following Kewley & Ellison (2008). The $H\alpha$ flux reported in the 3D-HST catalog is reduced by this ratio to determine the $H\alpha$ flux. This physically-motivated correction (typically around $\sim 25\%$ for our sample) is somewhat larger than the 20% usually assumed (Wuyts et al. 2011).

3 RESULTS

Figure 4 shows the ratio between $H\alpha$ and UV SFR measurements (which we refer to as $\eta = \log[SFR_{H\alpha}/SFR_{UV}]$) as a function of the offset between the UV SFR and the Whitaker et al. (2014) main sequence (ΔMS), color coded by their location in UVJ space (Wuyts et al. 2007; Williams et al. 2009) using the Whitaker et al. (2012) definition. As expected, both SFR measures agree for galaxies with ongoing star formation. As galaxies drop below the main sequence, more systems have low or undetected $H\alpha$ emission as the instantaneous SFR (traced by $H\alpha$) decreases more quickly than the average SFR (traced by UV). However, there remains a significant population of systems with η close to 0. Notably, 11% of UVJ -quiescent objects and 20% of objects more than 1 dex below the main sequence have significant $H\alpha$ emission.

While UVJ -quiescent objects with $H\alpha$ emission have higher $E(B-V)$ values than UVJ -quiescent objects on average, most are characterized by $E(B-V) < 0.1$, suggesting that they are generally not dusty contaminants. Significant $24\mu m$ emission is present in only 24% of UVJ -quiescent objects and 48% of objects more than 1 dex below the main sequence. Although there remains uncertainty regarding the amount of $24\mu m$ emission that originates from old stars, the $24\mu m$ luminosities of objects with $24\mu m$ emission can generally be accounted for with a combination of low level star formation (consistent with their dust-corrected UV SFRs) and emission from an old stellar population (Leroy et al. 2012; Salim et al. 2007; Kelson & Holden 2010). Altogether, although dusty contaminants may be present in our sample, they likely don't represent a significant source of contamination for our study.

Galaxies on the main sequence are consistent with $\eta = 0$ and have a small (~ 0.2 dex) scatter in η , but the distribution of $H\alpha$ fluxes and non-detections among galaxies below the main sequence implies evolution of η as systems fall off of the main sequence. Assuming η is normally distributed, the mean and standard deviation of that distribution that best-fit the distribution of $H\alpha$ fluxes and non-detections among low-SFR galaxies is -0.8 and 0.7 dex respectively.

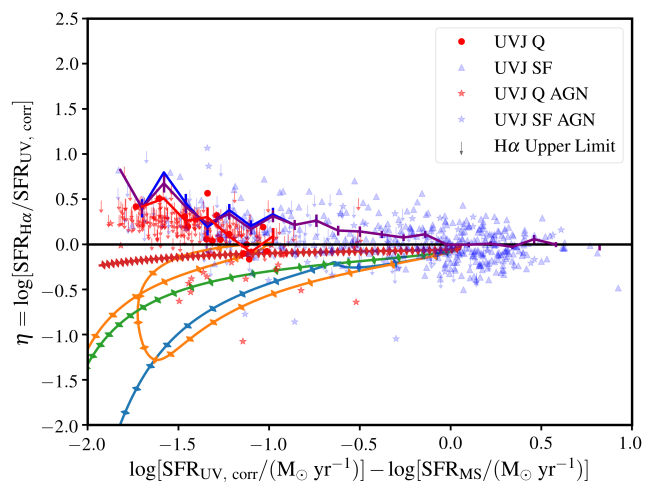


Figure 4. The relationship between η and ΔMS for galaxies in our sample. Galaxies are color-coded by whether they are classified as star-forming (blue) or quiescent (red) based on the UVJ diagram. The blue, red, and purple lines show the binned relationship between η and ΔMS for UVJ -star-forming, UVJ -quiescent, and all objects with $H\alpha$ detections respectively. Arrows illustrate the 3σ limits of galaxies without a significant $H\alpha$ detection. Although we do not include X-ray detected AGN in our primary sample, we show them here as stars to illustrate their distribution in this space. Star-forming galaxies with AGN actually have similar η values compared with galaxies without significant AGN, whereas quiescent galaxies with AGN have slightly less $H\alpha$ emission than galaxies without AGN. Solid ticked lines illustrate how a galaxy following different star-formation histories would evolve in this space, with ticks every 75 Myr (see Sec. 3). In agreement with previous studies, $H\alpha$ and UV SFRs match closely for galaxies on the main sequence. However, a substantial amount of scatter is present for galaxies below the main sequence. This scatter can only be reproduced with a bursty star-formation history.

To address the possibility that this $H\alpha$ emission is from bursty star formation, we illustrate how η evolves as a function of ΔMS for various model star-formation histories (SFHs). All models are based on an exponentially declining plus exponential burst star-formation history following a period of constant SFR of the form:

$$SFR(t) = SFR_0 e^{-(t-t_q)/\tau_0} + \delta e^{-|t-t_q-t_1|/\tau_{burst}}, \quad (4)$$

where SFR_0 is the SFR of the galaxy before quenching occurs, t_q is the time when the galaxy quenches, τ_0 is the quenching timescale, δ is the peak burst amplitude, t_1 corresponds to when the burst occurs after the initial quenching, and τ_{burst} is the characteristic timescale of the burst. First, we consider two bursty models with $\tau_{burst} = \tau_0 = 100$ Myr and $\delta = 1 M_{\odot} yr^{-1}$: models A and B have $t_1 = 0.3$ Gyr and $t_1 = 1.25$ Gyr respectively. Although τ_0 is not constrained in general, our choice of $\tau_0 \sim 100$ Myr is motivated by studies of recently quenched galaxies finding stellar ages consistent with short timescales (Zick et al. 2018; French et al. 2018; Belli et al. 2019). Additionally, we consider two no-burst models to compare with our bursty models. Model C is a smooth model with $\tau_0 = 200$ Myr and closely resembles model A in most other aspects. Model D, which is characterized by $\tau_0 = 1$ Gyr, represents the null hypothesis of quenching too slow to alter the $H\alpha/UV$ SFR ratio (models with τ_0 longer than the ~ 200 Myr lifetime of a B star quickly resemble the 1 Gyr model). These models are summarized in Table 1. For each SFH, we model the stellar population using the PYFSPS code (Conroy et al. 2009; Conroy & Gunn 2010; Foreman-

Model	δ ($M_{\odot} \text{ yr}^{-1}$)	t_1 (Gyr)	τ_0 (Myr)	τ_{burst} (Myr)
A	1	0.3	100	100
B	1	1.25	100	100
C	0	–	200	–
D	0	–	1000	–

Table 1. The parameters of the model SFHs used in our analysis.

Mackey et al. 2014). We initialize all models with 5 Gyr of continuous star formation at $10 M_{\odot} \text{ yr}^{-1}$ (mimicking the formation of a $\sim 10^{10} M_{\odot}$ galaxy to match the initial colors and UV luminosities), after which point, $\text{SFR}(t)$ follows Equation 4. The models all have a solar metallicity and a Chabrier IMF. The adoption of a higher metallicity could change the inferred UV SFR, but the η distribution of systems with $10^{10} \leq M_* < 10^{10.75} M_{\odot}$ is statistically identical to the η distribution of systems with $M_* \geq 10^{10.75} M_{\odot}$ among transition population (systems 1 – 1.75 dex below the main sequence). This evidence, combined with the fact that stellar metallicity is observed to vary by less than 0.2 dex across our the mass range of our sample for low-SFR galaxies (Choi et al. 2014; Estrada-Carpenter et al. 2019), suggests that the adoption of a uniform solar metallicity for our models is not unrealistic. From the synthesized spectra, the UV and H α SFRs are calculated according to equations 1 and 2, respectively. These models are not meant to span the entire range of plausible scenarios; rather they give a general sampling of what different quenching models predict.

These star-formation histories are summarized in Figure 5. As seen in Figure 4, η decreases dramatically with increasing ΔMS for all models with $\tau_0 \leq 200$ Myr. For $\tau_0 = 1$ Gyr, η remains roughly constant during the quenching process. The bursty models are distinguished by a sharp increase in η during the burst due to H α emission from young stars. In particular, bursty SFHs predict a large range of η for low SFRs present in the data, while smooth SFHs predict a narrow range of η values at a given UV SFR.

4 MODELING THE TRANSITION POPULATION

To test which SFH model best matches the observations, we model the expected H α flux distribution among galaxies between 1 and 1.75 dex below the main sequence. For each model SFH described above, we construct an expected H α flux distribution based on the objects in our sample. Specifically, we determine the expected H α flux for each object given its UV SFR and the η value predicted by each particular SFH as follows:

- (i) For each galaxy in our sample, the initial SFR (SFR_0) is taken to be the SFR of a galaxy with the same stellar mass and redshift on the Whitaker et al. (2014) main sequence plus normally-distributed scatter of 0.3 dex.
- (ii) The value of η is estimated from the assumed SFH and the observed UV SFR. The ratio between the observed UV SFR and SFR_0 is taken to be SFR/SFR_0 in equation 4 and used to determine t , which is in turn used to determine η (see Fig. 5). In the case that this results in multiple values of η , the dereddened diagonal UVJ color ($C_{\text{SED}} = 0.82(U - V) - 0.57(V - J)$, from Fang et al. 2018) of the galaxy is compared with the model C_{SED} at the various times. The time with the closest color to the observed galaxy is used. The H α SFR is determined from the η value and the dust-corrected UV SFR.

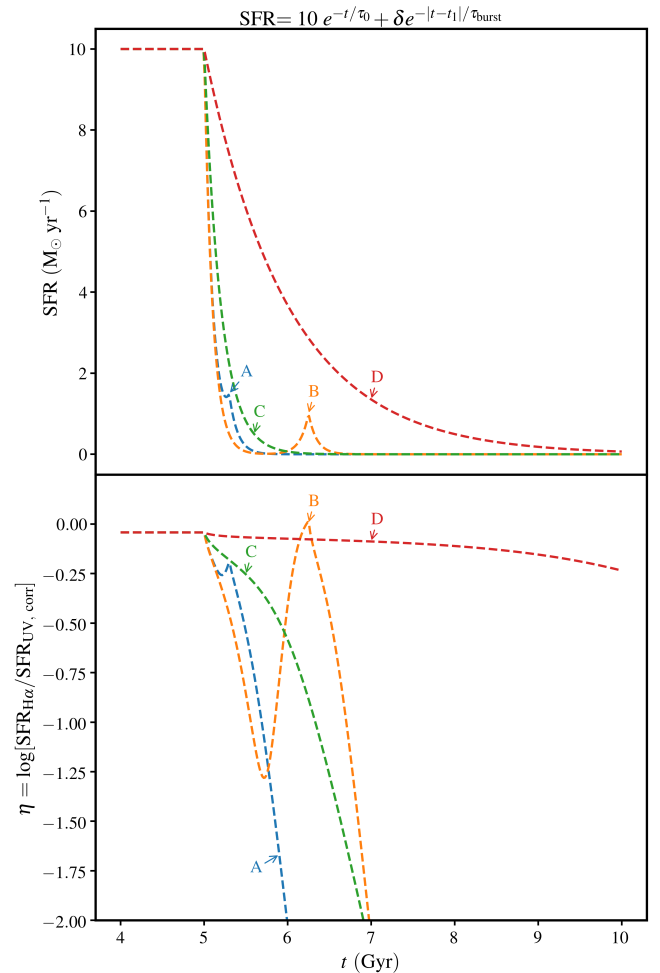


Figure 5. An illustration of the model SFHs used in this analysis. **Top:** The SFR as a function of time for our models. Models A, B, and C experience a rapid decline in star formation activity. Bursty models A and B experience exponential bursts of $1 M_{\odot} \text{ yr}^{-1}$, with both the quenching and the burst characterized by 100 Myr timescales. Models C and D describe a smooth quenching process with $\tau_0 = 200$ Myr and $\tau_0 = 1$ Gyr respectively. **Bottom:** The ratio of H α -to-UV SFR indicators as a function of time for our models. For slow quenching (model D), η does not evolve substantially, whereas the rapid shutdown of star-formation in models A-C results in a correspondingly rapid decrease in H α emission. This, accompanied by the slower decrease of UV emission results in quickly decreasing η values. However, during bursts the H α emission quickly rejuvenates.

- (iii) The H α SFR is converted to an H α luminosity.
- (iv) Absorption at H α is subtracted from the H α luminosity following Equation 3 using the bolometric light-weighted age as t_{LW} .
- (v) Emission from AGB stars is added to the H α luminosity as $2 \times 1.37 \times 10^{29} \text{ erg s}^{-1} M_{\odot}^{-1}$ times the observed stellar mass (the factor of 2 accounts for [NII] emission from AGB stars, which is characterized by an [NII]/H α ratio of 1).
- (vi) The H α luminosity is corrected for attenuation and [NII] contamination with the same prescriptions as described in Section 2.
- (vii) This luminosity is converted to flux, and a normally-distributed error of $\sigma = 8 \times 10^{-18} \text{ erg/s/cm}^2$ is added to this measurement (Momcheva et al. 2016).

Although X-ray-detected AGN are excluded from our sample, we include the effects of any X-ray-non-detected AGN in our model. Using the mass and redshift-dependent AGN luminosity functions of Aird et al. (2012), we predict the fraction of our subsample expected to host AGN. We take the difference between the expected AGN occurrence and the number of observed AGN as the number of X-ray-non-detected AGN. This number of galaxies is randomly selected from our sample, and for each supposed non-detected AGN, we replace the $H\alpha$ luminosity expected from the SFH model with the $H\alpha$ luminosity expected given the $H\alpha/UV$ ratio of a randomly chosen X-ray-detected AGN. Undetected AGN represent 10% of our subsample and their $H\alpha/UV$ ratios are not substantially different than the non-AGN population, so this correction does not have a substantial impact on the analysis. Additionally, excluding AGN based on their IRAC colors, which is more sensitive to extremely dust-extinguished AGN compared with X-ray-AGN (Stern et al. 2005), does not affect our conclusions.

Figure 6 illustrates the distributions of $H\alpha+[NII]$ flux for both the observations (solid histogram) and the models (hatched histograms) for galaxies between 1 and 1.75 dex below the main sequence. Also shown are the results of an Anderson Darling test comparing the predicted $H\alpha$ distributions with observations. For this test, all objects with $H\alpha$ flux less than $10^{-16.5} \text{ erg s}^{-1} \text{ cm}^{-2}$ are considered non-detections and considered to have 0 flux. The slow quenching model (model D) substantially overpredicts the number of $H\alpha$ detections. On the other hand, while the faster smooth model (model C) only slightly underpredicts the number of $H\alpha$ detections, it significantly underpredicts the observed flux for these objects. The quick burst of model A means that by the time the UV SFR is below the main sequence, η values quickly and uniformly fall, such that it underpredicts the $H\alpha$ flux throughout this sample. The large degree of variation in η in model B, however, is able to reproduce the large variation in $H\alpha$ fluxes apparent in our sample.

4.1 Rest-Frame Colors

As an independent test of the SFHs of $z \sim 1$ galaxies, we compare the η values with rest-frame, de-reddened $U - V$ colors in Figure 7. Again, we find that blue star-forming galaxies have η values close to 0, whereas red quiescent galaxies have a wide range of η values. In Figure 8, we show the $H\alpha$ distributions produced through the same method as Figure 6, but with $U - V$ color in place of UV SFR. For objects with $1.5 < U - V < 2$, where 88% of objects more than 1 dex below the main sequence live, the $H\alpha$ distribution is again most consistent with bursty model B.

5 DISCUSSION

In this analysis, we find that a bursty SFH is required in order to reproduce the large range in the $H\alpha/UV$ ratios of galaxies with low SFRs. In this section we discuss a few possible origins of this result. First, we discuss the effect of various systematics related to measuring/interpreting the $H\alpha$ and UV SFRs of galaxies in our sample. Next, we discuss possible physical mechanisms driving the range of η values observed in our sample.

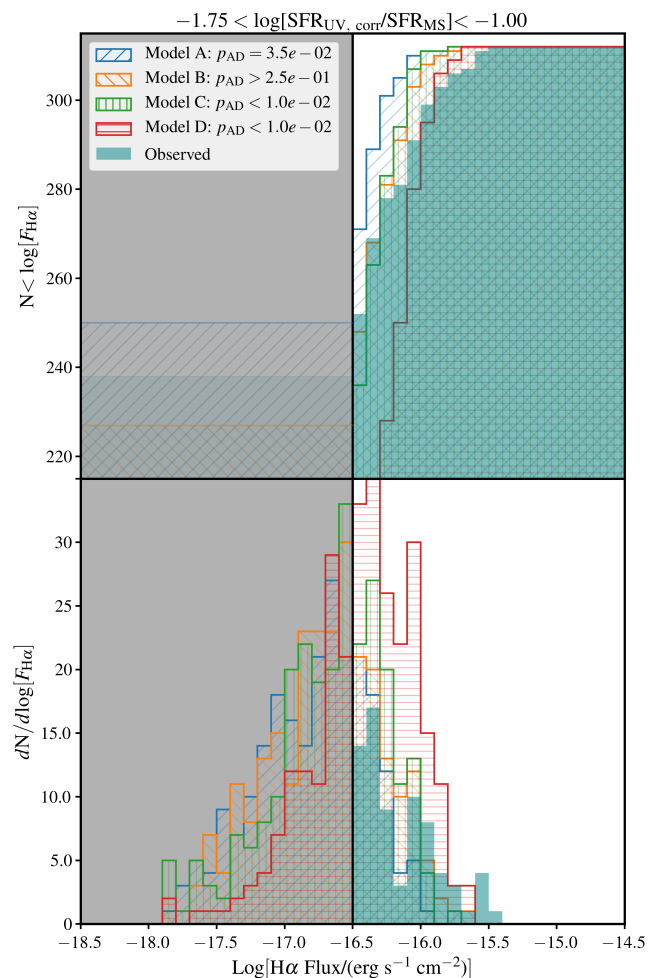


Figure 6. Bottom: The expected $H\alpha$ flux distribution (hatched distributions) for our various SFHs compared with observations (solid distribution) for objects with UV SFRs between 1 and 1.75 dex below the main sequence. For clarity, non-detections, which represent the majority of the sample, are not shown. Objects with $H\alpha$ flux below $10^{-16.5} \text{ erg s}^{-1} \text{ cm}^{-2}$ (shaded region) are also considered non-detections. **Top:** The corresponding cumulative distributions. In the legend, we show the Anderson-Darling p values comparing the theoretical distribution with the observed one (capped at 0.01 and 0.25). The bursty model B best represents the observed distribution. On the other hand, the smooth quenching model (model C), and the model with a burst shortly after quenching (model A) do not produce enough $H\alpha$ emission to match the observations, and the slow quenching model (model D) produces too many $H\alpha$ detections compared with the observations.

5.1 Systematics

5.1.1 Emission from Active Galactic Nuclei

While we account for X-ray AGN in our analysis, it is possible that low-luminosity or obscured AGN contribute to the $H\alpha$ emission of these sources. Indeed Belli et al. (2017) have found that a number of UVJ -quiescent objects with $H\alpha$ emission have $[NII]/H\alpha$ ratios consistent with an AGN. However, for a wide range of UV luminosities, the inferred $H\alpha$ and UV SFRs are in agreement (see Fig. 4), so there is no reason to believe that low-level AGN present a significant bias in our modeling. Additionally, X-ray non-detected AGN are not expected to represent a substantial fraction of our

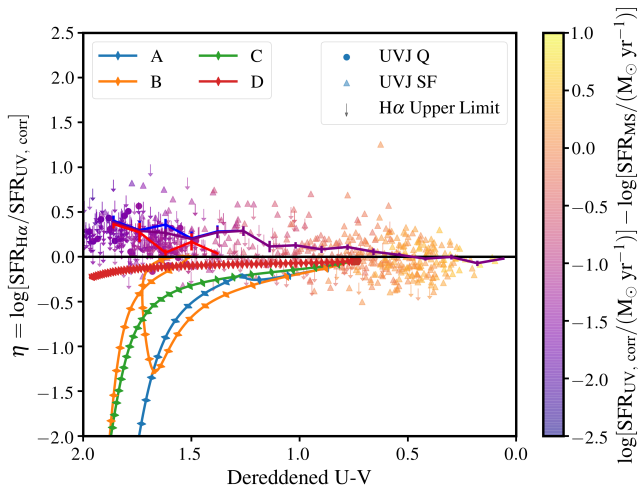


Figure 7. The $H\alpha$ -to-UV ratio as a function of dereddened $U - V$ color. The points are color-coded by the UV SFR. As with Figure 4, star-forming galaxies have η values close to 0, but the distribution of $H\alpha$ SFRs among red galaxies implies a wide range of η values. As with Figure 4, ticked lines represent the evolution of our models through this space, with ticks every 75 Myr.

sample, further suggesting that the presence of an AGN does not significantly affect our conclusions.

5.1.2 Emission from Evolved Stars

UV emission from evolved stars is apparent in local elliptical galaxies (Dorman et al. 1995). Studies of the spectra and colors of these galaxies suggest that this emission is primarily due to post-AGB and Blue-Horizontal-Branch stars (Yan 2018). This emission is nominally included in the P_YFSPS models, but significant uncertainties remain in our understanding of this phase of stellar evolution, so our models may be underestimating the UV luminosity of evolved stellar populations. However, this uncertainty does not affect our conclusions: if evolved stars contribute more UV emission than our models, our models should move down and to the right in Figure 4 *except for during a burst*, during which UV emission is dominated by young stars and the contribution from evolved stars is negligible. In this case, smooth models would be a worse fit to the η distribution, whereas bursty models would better fit the distribution.

5.1.3 Extra Extinction Around HII Regions

A significant source of uncertainty regarding this analysis is the amount of extra extinction around HII regions. Because the relationship between stellar and nebular extinction solely affects the $H\alpha$ SFR, adjusting this ratio would directly alter our results. However, while this relationship is important to ensure that both SFR measures agree for star-forming galaxies, the median $H\alpha$ extinction value for quiescent objects is only 0.3, so extinction does not play a very important role in calculating the SFRs of the low-SFR population. If we adopt the slightly higher nebular-to-continuum extinction ratio (known as the f factor) from Calzetti et al. (2000), model C fits the observations slightly better, but our model B remains the best fitting model. Adopting a lower nebular-to-continuum ratio, as suggested by some recent high- z studies (for ex. Puglisi et al. 2016;

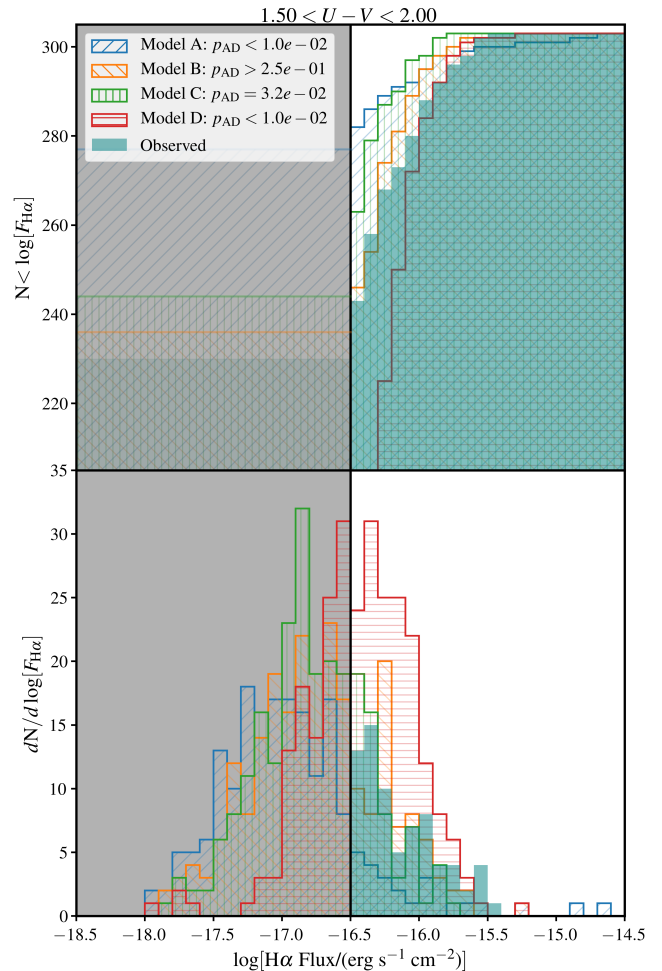


Figure 8. Bottom: We compare the observed $H\alpha$ flux distribution with our models for systems with dereddened $U - V$ colors between 1.5 and 2. **Top:** The corresponding cumulative distribution, with the legend showing the results of Anderson-Darling tests between the models and data. Again, bursty model B best matches the observed $H\alpha$ distribution. As with Figure 6, the shaded region below $F_{H\alpha} = 10^{-16.5}$ erg s $^{-1}$ cm $^{-2}$ highlights objects considered non-detections.

Broussard et al. 2019), improves the fit of model A and weakens the fit of model B. However, using a lower ratio overestimates η for systems on the star-forming main sequence: adopting an f factor of 1 changes the median η value among objects within 0.3 dex of the main sequence from -0.06 to -0.39 . The suggested variation in f factor at higher redshift is driven by dusty objects with high SFRs (Reddy et al. 2015), whereas our sample has sSFRs more similar to low- z objects. Observations of local galaxies suggest that low-sSFR galaxies that have Calzetti-like f factors, whereas high sSFR galaxies (like those at high z) have lower f factors (Battisti et al. 2016). Additionally, the agreement between Balmer-decrement-based measurements and our $A_{H\alpha}$ measurements, as well as the fact that η is not correlated with extinction among our sample, suggests that this is not a significant issue (see Fig. 3).

5.1.4 Contamination from [NII]

Contamination from nearby [NII] represents a non-negligible contribution to the observed flux (and inferred η values). If the

[NII]/H α ratio is substantially higher among our sample, the inferred η values could be overestimated. Indeed, [NII] emission from high- z galaxies appears higher than expected given their [OIII]/H β ratios (Steidel et al. 2014; Masters et al. 2014; Jones et al. 2015; Shapley et al. 2015, but see Sanders et al. 2018). Increasing the [NII]/H α ratio by 0.37 dex increases the predicted flux distribution, bringing models A and C in better agreement with observations. The [NII] offset appears to be constant with SFR (Strom et al. 2017), which would induce a roughly constant shift in η for all SFRs, not a preferentially lower η for low-SFR galaxies in particular, as would be necessary for our measurements to match a smoothly declining SFH. Furthermore, there is no residual trend between η and stellar mass, as one would expect if this metallicity-dependent effect was important.

5.2 Physical Mechanisms

5.2.1 Initial Mass Function

As H α emission primarily is dominated by stars with $> 8 M_{\odot}$, whereas UV emission originates from stars with $> 4 M_{\odot}$, the ratio of the two SFR measures is sensitive to the initial mass function (IMF) of the stellar population. In particular, Fumagalli et al. (2011) and da Silva et al. (2014) have suggested that stochastic sampling of the initial mass function, both due to limited mass and time resolution at low SFRs may be responsible for variation in H α /UV SFRs. To test the impact of stochastic IMF sampling on our model, we utilize the SLUG code (Krumholz et al. 2015). Contrary to traditional stellar-population synthesis codes which integrate a given IMF to a certain mass regardless of the overall SFR, this code directly and stochastically samples the IMF to generate stellar populations. However, the dispersion in the H α to UV ratio for a model with an SFR of $0.1 M_{\odot} \text{ yr}^{-1}$ (corresponding to $\Delta\text{MS} \sim -2$) is only 0.1 dex (with the fraction of stars formed in clusters set to 1), not enough to explain the large dispersion in η values.

Alternatively, a very top-heavy IMF could result in systematically higher η values compared with the Chabrier values. We test this hypothesis using the van Dokkum (2008) parameterization of the IMF, with M_c set to 1.5 (at the high end of what is observed). In this case, UV and H α emission decrease at similar rates, even for the fast quenching models, such that no model is able to reproduce the large number of galaxies with low η values. The primary effect of adopting a more-bottom heavy IMF (as suggested by some observations of nearby massive ellipticals van Dokkum et al. 2017) is a decrease in UV and H α emission at a given SFR. Still, the large dispersion in H α SFRs for galaxies with low UV SFRs cannot be reproduced by any smooth quenching model and is best reproduced by model B. Similarly, an integrated galactic-IMF (IGIMF), in which stars are formed primarily in clusters (Weidner & Kroupa 2005; Weidner et al. 2011), results in more top-heavy for galaxies with lower SFRs. Following Pflamm-Altenburg et al. (2007), we adjust the H α -to-SFR ratio for their *Minimal-1* and *Standard* models. However, for both models, the variation of the H α luminosity with SFR is not sufficient to explain the observed variation and no SFH model matches the observed distribution with a p value higher than 0.02.

5.2.2 Minor Mergers

Within massive galaxies, bursty star formation is often thought of as due to minor mergers or interactions (Mihos & Hernquist 1994; Somerville et al. 2008). For $M_* = 10^{10} M_{\odot}$ galaxies at $z \sim 1$, the

major merger rate is $10^{-4} \text{ Mpc}^{-3} \text{ Gyr}^{-1}$ (Duncan et al. 2019), corresponding to $\sim 10\%$ per galaxy per Gyr. Assuming that minor merger rate is a factor of 10 higher than the major merger rate (Rodríguez-Gomez et al. 2015), we would minor mergers to be common among our sample. This suggests that minor mergers driving bursty star formation could explain the observed burstiness in our population.

6 CONCLUSIONS

Using data from the 3D-HST survey, we analyze H α emission within ~ 800 massive galaxies at $z \sim 1$, focusing on galaxies undergoing the transition between star-forming and quiescence to better understand the process of quenching in these galaxies. Our conclusions are as follows.

- In contrast with expectations, we find evidence of H α emission for galaxies down to the lowest levels of UV SFR present in our sample, including 11% of systems identified as quiescent through the *UVJ* diagram.
- There is a large dispersion (~ 0.7 dex) in the ratio between H α and UV SFRs for galaxies with low UV SFRs. Even after accounting for the expected emission from AGN and evolved stars, this large range is inconsistent with a smoothly declining star-formation history.
- The observed variation in H α -to-UV SFRs among massive galaxies in the process of quenching implies that quenching at $z \sim 1$ is not characterized by a continuous decline in SFR. On the contrary, by modeling various bursty and non-bursty star-formation histories, we show that, bursty star formation continues as the SFR declines.

Our analysis has been limited to high-mass systems due to the limited S/N of lower mass systems, but given that they have bursty star formation when they are star forming, an analysis of the H α emission in low-mass galaxies transitioning to quiescence would be particularly valuable.

ACKNOWLEDGMENTS

We are grateful to the anonymous reviewer, whose suggestions greatly improved this paper. This research made use of *Astropy*, a community-developed core Python package for Astronomy (Astropy Collaboration et al. 2013). Additionally, the Python packages *NumPy* (Walt et al. 2011), *iPython* (Prez & Granger 2007), *SciPy* (Jones et al. 2001), and *matplotlib* (Hunter 2007) were utilized for the majority of our data analysis and presentation.

APPENDIX A: OTHER STAR-FORMATION HISTORIES

While it is beyond the scope of this work to evaluate all possible bursty SFHs, we explore the effects of varying the burst timescale, delay time, and strength in this appendix. In Table A1, we describe 4 SFHs that we explore beyond the 4 described in our primary analysis in the form of

$$\text{SFR} = \text{SFR}_0 e^{-(t-t_q)/\tau_0} + \delta e^{|t-t_q-t_1|/\tau_{\text{burst}}}, \quad (\text{A1})$$

with δ representing the burst amplitude, t_q representing the time of quenching, t_1 representing the burst delay time, and τ_{burst} representing the exponential timescale of the burst.

Figure A1 shows the relationship between η and ΔMS for

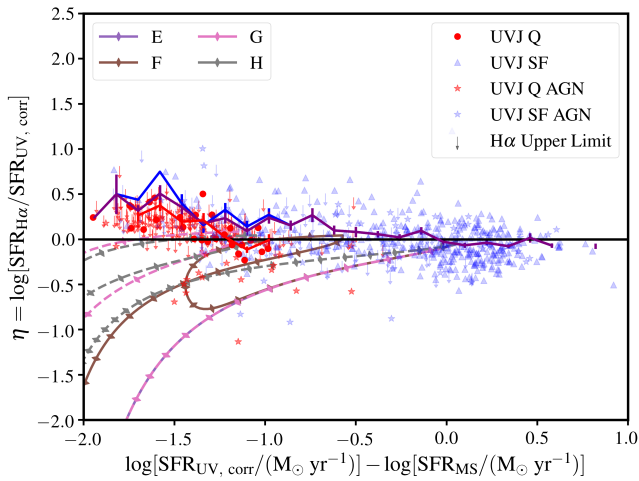


Figure A1. The evolution of η with ΔMS for SFH models E–H.

these SFHs in comparison with our observations. The most important variable is the burst delay time: models with high t_1 values are able to reach lower SFR values before bursting. As shown in Figure A2, bursty model F is preferred to any smoothly declining model.

We also consider linearly increasing, delayed, and inverted tau models in the form of:

$$\text{SFR}(t) = \begin{cases} \text{SFR}_0(t/t_1) & t < t_1 \\ \text{SFR}_0 e^{-t/\tau_0} + \delta e^{-|t-t_1|/\tau_{\text{burst}}} & t > t_1, \end{cases} \quad (\text{A2})$$

$$\text{SFR}(t) = \text{SFR}_0(t-t_1)e^{-(t-t_1)/\tau_0} + \delta e^{-(t-t_1)/\tau_{\text{burst}}}, \quad (\text{A3})$$

and

$$\text{SFR}(t) = \begin{cases} \text{SFR}_0 e^{t/\tau_1} & t < t_1 \\ \text{SFR}_0 e^{-t/\tau_0} + \delta e^{-|t-t_1|/\tau_{\text{burst}}} & t > t_1, \end{cases} \quad (\text{A4})$$

with SFR_0 , δ , t_1 , τ_0 , and τ_{burst} values as in models A, B, C, and D. The parameters describing these models as well as the results of our comparison of these models with observations are found in Table A1. For the delayed model (equation A3), no model accurately reproduces the $H\alpha$ flux distribution for objects between 1 and 1.75 dex below the main sequence. For the inverse model (equation A4), bursty model B reproduces the $H\alpha$ flux distribution, whereas smooth model C does not. Lastly, for the linearly increasing model (equation A2), both model B and C reproduce the observed $H\alpha$ flux distribution for objects between 1 and 1.75 dex below the main sequence. Model B fits the $H\alpha$ distribution for objects with dust-corrected $U-V$ colors between 1 and 2 and model C does not, however. In summary, regardless of the general form of the star-formation history adopted in our models, a bursty star-formation history better fits the observed $H\alpha$ fluxes compared with a smoothly-declining star-formation history.

REFERENCES

- Aird J., et al., 2012, *ApJ*, 746, 90
 Astropy Collaboration et al., 2013, *A&A*, 558, A33
 Balogh M. L., Baldry I. K., Nichol R., Miller C., Bower R., Glazebrook K., 2004, *ApJ*, 615, L101
 Battisti A. J., Calzetti D., Charly R. R., 2016, *ApJ*, 818, 13

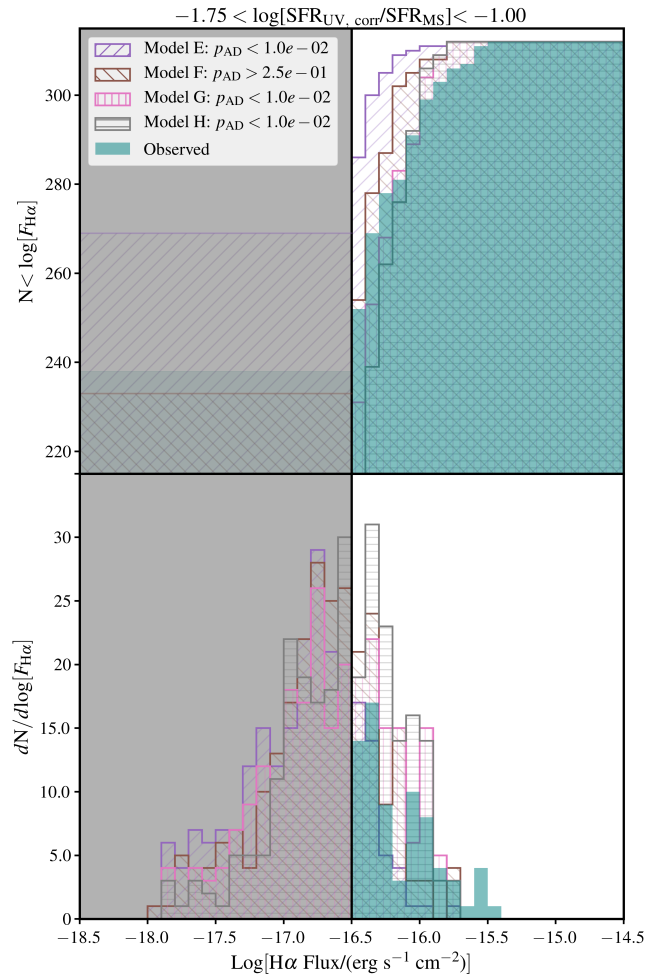


Figure A2. The $H\alpha$ flux distribution for SFH models E–H. Even considering the additional models here, it is clear that bursty models fit the observations better than smooth models overall.

- Beckmann R. S., et al., 2017, *MNRAS*, 472, 949
 Belfiore F., et al., 2016, *MNRAS*, 461, 3111
 Bell E. F., et al., 2004, *ApJ*, 608, 752
 Belli S., et al., 2017, *ApJ*, 841, L6
 Belli S., Newman A. B., Ellis R. S., 2019, *ApJ*, 874, 17
 Brammer G. B., van Dokkum P. G., Coppi P., 2008, *ApJ*, 686, 1503
 Broussard A., et al., 2019, *ApJ*, 873, 74
 Calzetti D., Armus L., Bohlin R. C., Kinney A. L., Koornneef J., Storchi-Bergmann T., 2000, *ApJ*, 533, 682
 Carnall A. C., McLure R. J., Dunlop J. S., Davé R., 2018, *MNRAS*, 480, 4379
 Ceverino D., Klypin A., 2009, *ApJ*, 695, 292
 Chabrier G., 2003, *PASP*, 115, 763
 Choi J., Conroy C., Moustakas J., Graves G. J., Holden B. P., Brodwin M., Brown M. J. I., van Dokkum P. G., 2014, *ApJ*, 792, 95
 Cid Fernandes R., Stasińska G., Mateus A., Vale Asari N., 2011, *MNRAS*, 413, 1687
 Conroy C., Gunn J. E., 2010, *ApJ*, 712, 833
 Conroy C., Gunn J. E., White M., 2009, *ApJ*, 699, 486
 Croton D. J., et al., 2006, *MNRAS*, 365, 11
 Daddi E., et al., 2005, *ApJ*, 626, 680
 Dekel A., Birnboim Y., 2006, *MNRAS*, 368, 2
 Di Matteo T., Springel V., Hernquist L., 2005, *Nature*, 433, 604
 Dorman B., O’Connell R. W., Rood R. T., 1995, *ApJ*, 442, 105
 Duncan K., et al., 2019, *ApJ*, 876, 110

Model	SFH Equation	δ ($M_{\odot} \text{ yr}^{-1}$)	t_1 (Gyr)	τ_0 (Myr)	τ (Myr)	p value (ΔMS)	p value (dereddened $U - V$)
E	4	0	–	100	–	< 0.01	< 0.01
F	4	3	1	100	100	> 0.25	< 0.01
G	4	1	1	200	200	< 0.01	< 0.01
H	4	3	1	200	200	< 0.01	< 0.01
A Increasing	A2	1	0.3	100	100	< 0.01	< 0.01
B Increasing	A2	1	1.25	100	100	> 0.25	0.11
C Increasing	A2	0	–	200	–	0.16	< 0.01
D Increasing	A2	0	–	1000	–	< 0.01	< 0.01
A Delayed	A3	1	0.3	100	100	< 0.01	< 0.01
B Delayed	A3	1	1.25	100	100	< 0.01	< 0.01
C Delayed	A3	0	–	200	–	< 0.01	< 0.01
D Delayed	A3	0	–	1000	–	< 0.01	< 0.01
A Inverse	A4	1	0.3	100	100	0.035	< 0.01
B Inverse	A4	1	1.25	100	100	> 0.25	> 0.25
C Inverse	A4	0	–	200	–	< 0.01	0.032
D Inverse	A4	0	–	1000	–	< 0.01	< 0.01

Table A1. The parameters of the model SFHs used in our extended analysis, along with the p value of an Anderson-Darling test comparing model systems with observations. Column 7 shows the comparison with objects between 1 and 1.75 dex below the main sequence and column 8 shows the p value resulting from the comparison with objects with dereddened U-V colors between 1.5 and 2.

- Estrada-Carpenter V., et al., 2019, *ApJ*, 870, 133
Faber S. M., et al., 2007, *ApJ*, 665, 265
Fang J. J., et al., 2018, *ApJ*, 858, 100
Foreman-Mackey D., Sick J., Johnson B., 2014, *python-fsps: Python bindings to FSPS (v0.1.1)*, doi:10.5281/zenodo.12157, <https://doi.org/10.5281/zenodo.12157>
French K. D., Yang Y., Zabludoff A. I., Tremonti C. A., 2018, *ApJ*, 862, 2
Fumagalli M., da Silva R. L., Krumholz M. R., 2011, *ApJ*, 741, L26
Fumagalli M., et al., 2014, *ApJ*, 796, 35
Galametz A., et al., 2013, *ApJS*, 206, 10
Goddard D., et al., 2017, *MNRAS*, 466, 4731
Gordon K. D., Clayton G. C., Misselt K. A., Landolt A. U., Wolff M. J., 2003, *ApJ*, 594, 279
Grogin N. A., et al., 2011, *ApJS*, 197, 35
Guo Y., et al., 2013, *ApJS*, 207, 24
Guo Y., et al., 2016, *ApJ*, 833, 37
Hahn C., Tinker J. L., Wetzel A., 2017, *ApJ*, 841, 6
Hopkins P. F., Hernquist L., Cox T. J., Di Matteo T., Robertson B., Springel V., 2006, *ApJS*, 163, 1
Hopkins P. F., Kereš D., Oñorbe J., Faucher-Giguère C.-A., Quataert E., Murray N., Bullock J. S., 2014, *MNRAS*, 445, 581
Hunter J. D., 2007, *Computing in Science & Engineering*, 9, 90
Ilbert O., et al., 2013, *A&A*, 556, A55
Jones E., Oliphant T., Peterson P., et al., 2001, *SciPy: Open source scientific tools for Python*, <http://www.scipy.org/>
Jones T., Martin C., Cooper M. C., 2015, *ApJ*, 813, 126
Kauffmann G., et al., 2003, *MNRAS*, 341, 33
Kelson D. D., Holden B. P., 2010, *ApJ*, 713, L28
Kennicutt R. C., Evans N. J., 2012, *ARA&A*, 50, 531
Kereš D., Katz N., Weinberg D. H., Davé R., 2005, *MNRAS*, 363, 2
Kewley L. J., Ellison S. L., 2008, *ApJ*, 681, 1183
Koekemoer A. M., et al., 2011, *ApJS*, 197, 36
Kriek M., van Dokkum P. G., Labbé I., Franx M., Illingworth G. D., Marchesini D., Quadri R. F., 2009, *ApJ*, 700, 221
Krumholz M. R., Fumagalli M., da Silva R. L., Rendahl T., Parra J., 2015, *MNRAS*, 452, 1447
Kuntschner H., et al., 2010, *MNRAS*, 408, 97
Leroy A. K., et al., 2012, *AJ*, 144, 3
Marigo P., Girardi L., Bressan A., Groenewegen M. A. T., Silva L., Granato G. L., 2008, *A&A*, 482, 883
Martig M., Bournaud F., Teyssier R., Dekel A., 2009, *ApJ*, 707, 250
Martin D. C., et al., 2007, *ApJS*, 173, 342
Masters D., et al., 2014, *ApJ*, 785, 153
Mihos J. C., Hernquist L., 1994, *ApJ*, 425, L13
Momcheva I. G., et al., 2016, *ApJS*, 225, 27
Muzzin A., van Dokkum P., Kriek M., Labbé I., Cury I., Marchesini D., Franx M., 2010, *ApJ*, 725, 742
Nandra K., et al., 2015, *ApJS*, 220, 10
Nayyeri H., et al., 2017, *ApJS*, 228, 7
Oppenheimer B. D., Davé R., 2006, *MNRAS*, 373, 1265
Pandya V., et al., 2017, *MNRAS*, 472, 2054
Peng Y.-j., et al., 2010, *ApJ*, 721, 193
Pflamm-Altenburg J., Weidner C., Kroupa P., 2007, *ApJ*, 671, 1550
Piovan L., Tantalò R., Chiosi C., 2003, *A&A*, 408, 559
Puglisi A., et al., 2016, *A&A*, 586, A83
Prez F., Granger B. E., 2007, *Computing in Science & Engineering*, 9, 21
Rangel C., Nandra K., Laird E. S., Orange P., 2013, *MNRAS*, 428, 3089
Reddy N. A., Erb D. K., Pettini M., Steidel C. C., Shapley A. E., 2010, *ApJ*, 712, 1070
Reddy N. A., et al., 2015, *ApJ*, 806, 259
Rodríguez-Gomez V., et al., 2015, *MNRAS*, 449, 49
Salim S., et al., 2007, *ApJS*, 173, 267
Salim S., et al., 2009, *ApJ*, 700, 161
Salvato M., et al., 2011, *ApJ*, 742, 61
Sanders R. L., et al., 2018, *ApJ*, 858, 99
Schawinski K., Thomas D., Sarzi M., Maraston C., Kaviraj S., Joo S.-J., Yi S. K., Silk J., 2007, *MNRAS*, 382, 1415
Schawinski K., et al., 2014, *MNRAS*, 440, 889

- Shapley A. E., et al., 2015, *ApJ*, 801, 88
- Shivaei I., Reddy N. A., Steidel C. C., Shapley A. E., 2015, *ApJ*, 804, 149
- Shivaei I., et al., 2017, *ApJ*, 837, 157
- Singh R., et al., 2013, *A&A*, 558, A43
- Skelton R. E., et al., 2014, *ApJS*, 214, 24
- Somerville R. S., Hopkins P. F., Cox T. J., Robertson B. E., Hernquist L., 2008, *MNRAS*, 391, 481
- Sparre M., Hayward C. C., Feldmann R., Faucher-Giguère C.-A., Muratov A. L., Kereš D., Hopkins P. F., 2017, *MNRAS*, 466, 88
- Stefanon M., et al., 2017, *ApJS*, 229, 32
- Steidel C. C., et al., 2014, *ApJ*, 795, 165
- Stern D., et al., 2005, *ApJ*, 631, 163
- Strom A. L., Steidel C. C., Rudie G. C., Trainor R. F., Pettini M., Reddy N. A., 2017, *ApJ*, 836, 164
- Thomas D., Maraston C., Schawinski K., Sarzi M., Silk J., 2010, *MNRAS*, 404, 1775
- Ueda Y., et al., 2008, *ApJS*, 179, 124
- Walt S. v. d., Colbert S. C., Varoquaux G., 2011, *Computing in Science & Engineering*, 13, 22
- Weidner C., Kroupa P., 2005, *ApJ*, 625, 754
- Weidner C., Kroupa P., Pflamm-Altenburg J., 2011, *MNRAS*, 412, 979
- Weisz D. R., et al., 2012, *ApJ*, 744, 44
- Wetzel A. R., Tinker J. L., Conroy C., van den Bosch F. C., 2013, *MNRAS*, 432, 336
- Whitaker K. E., van Dokkum P. G., Brammer G., Franx M., 2012, *ApJ*, 754, L29
- Whitaker K. E., et al., 2014, *ApJ*, 795, 104
- Whitaker K. E., et al., 2017, *ApJ*, 838, 19
- Wild V., Almaini O., Dunlop J., Simpson C., Rowlands K., Bowler R., Maltby D., McLure R., 2016, *MNRAS*, 463, 832
- Williams R. J., Quadri R. F., Franx M., van Dokkum P., Labbé I., 2009, *ApJ*, 691, 1879
- Wisnioski E., et al., 2019, arXiv e-prints, p. arXiv:1909.11096
- Worthey G., Ottaviani D. L., 1997, *ApJS*, 111, 377
- Wuyts S., et al., 2007, *ApJ*, 655, 51
- Wuyts S., et al., 2011, *ApJ*, 738, 106
- Wuyts S., et al., 2013, *ApJ*, 779, 135
- Xue Y. Q., et al., 2011, *ApJS*, 195, 10
- Yan R., 2018, *MNRAS*, 481, 476
- Zahid H. J., Dima G. I., Kudritzki R.-P., Kewley L. J., Geller M. J., Hwang H. S., Silverman J. D., Kashino D., 2014, *ApJ*, 791, 130
- Zick T. O., et al., 2018, *ApJ*, 867, L16
- da Silva R. L., Fumagalli M., Krumholz M. R., 2014, *MNRAS*, 444, 3275
- van Dokkum P. G., 2008, *ApJ*, 674, 29
- van Dokkum P. G., et al., 2015, *ApJ*, 813, 23
- van Dokkum P., Conroy C., Villaume A., Brodie J., Romanowsky A. J., 2017, *ApJ*, 841, 68
- van der Wel A., et al., 2016, *ApJS*, 223, 29